Available online at www.sciencedirect.com
SCIENCE DIRECT®
Journal of Computational Physics 200 (2004) 177–191
JOURNAL OF COMPUTATIONAL PHYSICS
www.elsevier.com/locate/jcp

# A formulation of Navier–Stokes problem in cylindrical coordinates applied to the 3D entry jet in a duct

F. Domenichini *, B. Baccani

*Dipartimento Ingegneria Civile, Università di Firenze, Via Santa Marta 3, 50139 Firenze, Italy*

Received 23 December 2003; received in revised form 24 March 2004; accepted 5 April 2004
Available online 7 May 2004

**Abstract**

A pseudospectral formulation of the three-dimensional Navier–Stokes equations in the cylindrical system of coordinates is presented, which automatically includes the regularity conditions at the polar axis for the Fourier harmonics. The mathematical system of equations is numerically implemented using standard methods for spatial discretisation and time advancement. The method presented here for incompressible flows can be easily extended to different set of equations and to different numerical schemes of various levels of accuracy. The formulation is applied to the solution of incompressible three-dimensional entry jets in a circular duct.


*Keywords:* Coordinate system singularity; Spectral methods; Navier–Stokes; Duct flows

## 1. Introduction

Several realistic fluid flows present one preferable direction and develop compactly about one axis, examples are numerous, from tube flows and jets to body wakes and vortex structures. The corresponding mathematical systems are often naturally written in the cylindrical system of coordinates. The choice of cylindrical coordinates, like any system that contains a symmetry axis, introduces singular terms in the governing equation of the type $r^{-n}$, being $r$ the radial coordinate and $n$ a positive exponent, typically $n = 1$ and $n = 2$, although the flow is continuous and regular at the axis.

A three-dimensional formulation of fluid flows in cylindrical coordinates requires the definition of appropriate boundary conditions at $r = 0$, notwithstanding the fact that it is not a physical boundary, that would guarantee the regularity of the flow. In the case of axisymmetric flows, the singular behaviour is simply cancelled by the symmetry condition at the axis. The strategy to deal with this difficulty in analytical approaches is commonly that of discarding the singular solutions among all the admissible ones (e.g. using the Bessel's functions of the first kind, and discarding those of the second kind).

* Corresponding author. Tel.: +39-55-4796321; fax: +39-55-495333.
*E-mail addresses:* federico@ingfi1.ing.unifi.it (F. Domenichini), bernardo.baccani@dicea.unifi.it (B. Baccani).

0021-9991/$ - see front matter 
doi:10.1016/j.jcp.2004.04.002

Several approaches have been proposed to remove properly the singularities from the numerical solutions in cylindrical coordinates, and well reproduce the behaviour close to the singular axis. A basic distinction must be made between finite-differences or finite-volume methods and methods that use a spectral decomposition along the azimuthal ($\theta$) direction about the singular axis. In finite-volume or finite-differences methods, different approaches have proven successful [1–4], generally based on several rigorous possibilities of avoiding the evaluation of some fluxes of the physical cell at $r = 0$. Mohseni and Colonius [5] eliminated the boundary at $r = 0$ by mapping the $[0\ 2\pi] \times [0\ R]$ polar domain into $[0\ \pi] \times [-R\ R]$.

The use of a spectral representation along the periodic coordinate $\theta$ is often to be preferred for the accurate solution of problems with simple geometry. In that case, the three-dimensional mathematical problem is transformed into a number of coupled two-dimensional ones for the spectral harmonics, on the meridian plane. However, each of such problems is characterised by singular terms whose degree of singularity grows with the harmonics. This is reflected by the number of regularity and boundary conditions that must be satisfied at the singular axis to allow a well-posed problem [6–10].

A possible approach in a spectral framework is the use of further spectral (polynomial) expansions in the radial direction too, using base functions that automatically satisfy the regularity conditions at $r = 0$. Chebyshev [11] and Jacobi polynomials have been used, also in conjunction with Legendre–Lagrangian ones and B-splines expansions [12–14]. These techniques are in principle very accurate although not commonly straightforward. On another side they cannot be easily generalised in other than the simplest cylindrical domains and boundary conditions.

In spectral methods, regularity conditions for the azimuthal harmonics are typically derived in the wavenumber space by using the properties at $r = 0$ of the functions chosen to expand velocity and pressure along the radial direction [9–12]. Pole conditions for Poisson-type equations in the physical space were derived by Huang and Sloan [15], and then used as numerical boundary conditions in a pseudospectral method. A different approach is introduced in [10], where the radial and azimuthal components of the velocity are substituted by two complex functions (which are their linear combinations, see also [11]), these are written in terms of the Cartesian velocities, and regularity conditions on the axis are derived using Taylor series; the numerical solution is obtained using a spectral-Galerkin method for the spatial discretisation in the meridian plane. A similar approach was developed by Constantinescu and Lele [9], and implemented in a finite-differences scheme to solve the equations at the singular axis. The Navier–Stokes equations are recast, at $r = 0$, by a set of equations for the coefficients of the radial Taylor expansions of the variables, resulting in the solution of low-dimensional linear systems. Substitution of the dependent variables has been also used in [8], based on the asymptotic behaviour of analytic functions in the limit $r \to 0$; the flow equations are discretised by using the Galerkin trigonometric approximation in azimuthal and streamwise directions and the Chebyshev collocation technique in $r$; the numerical solution is based on the influence matrix technique introduced in [6].

In the present work, a spectral formulation is proposed, following [7,9,10], where all the regularity conditions at the polar axis for the Fourier harmonics are automatically included. These conditions are satisfied by introducing a normalisation of each harmonics with powers of the radial distance, say $r^n$, being $n$ an exponent related to the harmonic number. The normalised harmonics have simple boundary conditions at the axis that automatically cancel the singular behaviour, similarly to what happens in the axisymmetric case. Such a normalisation allows writing a mathematically well-posed problem up to the singular axis, while the boundary conditions far from the axis itself are simply rewritten. The new mathematical system, that is equivalent to the original one plus the regularity conditions, is a regular one. It can be used in analytical studies and it is particularly useful in numerical solutions.

In the present numerical solutions centred finite differences are used in the meridian plane with second-order accuracy, and an explicit fractional step method is employed. However, the numerical technique is out of the scope of this article, because the approach described here is independent on the specific numerical method adopted and it can be employed with higher order spatial schemes or implicit time advancements.

The mathematical formulation and the numerical method are reported in Sections 2 and 3, respectively; results of different test cases are discussed in Section 4, concluding remarks can be found in Section 5.

## 2. Spectral formulation of the Navier–Stokes equation in cylindrical coordinates

The vector dimensionless form of the incompressible Navier–Stokes equations can be written as

$$\frac{\partial \mathbf{v}}{\partial t} - \mathbf{v} \times \boldsymbol{\omega} = -\nabla \phi - \frac{1}{Re} \nabla \times \boldsymbol{\omega}, \tag{1a}$$

$$\nabla \cdot \mathbf{v} = 0. \tag{1b}$$

The vectors $\mathbf{v}$ and $\boldsymbol{\omega}$ are the velocity and vorticity, respectively. The scalar field $\phi$ represents the irrotational contribution to the flow, that is $\phi = p + v^2/2$, where $p$ is the dimensionless pressure field and $v$ is the velocity modulus. The parameter Re is the Reynolds number $Re = UL/v$, where the physical scales $U$ and $L$ depend on the specific problem under examination, and $v$ is the kinematic viscosity of the fluid.

Consider the cylindrical system of coordinates $\{z, r, \theta\}$; the definition of the corresponding differential operator in (1) can be found in [16]. The axisymmetric arrangement of the coordinate system suggests expanding any variable in Fourier series along $\theta$ as $f(z, r, \theta, t) = \sum f_n(z, r, t) \mathrm{e}^{\mathrm{i}n\theta}$. Introduction of the Fourier representations in equations (1) give the evolving equation for each harmonic. Whereas the equations will be completed with the boundary-conditions appropriate for each specific problem, the treatment of the axis, $r = 0$, requires particular attention, because the condition of continuity of the variables and their derivatives must be guaranteed by the spectral representation.

Following [9], the flow variables are expanded in Taylor series along the radial coordinate, giving the polynomial expression of each harmonic of single-valued, $v_z$ and $\phi$, or multivalued variables, $v_r$ and $v_\theta$. The regularity conditions at $r = 0$ for a single-valued function, say $v_z$, can be written in compact form as [7,10]

$$\frac{\partial^k v_{zn}}{\partial r^k} = 0, \quad n > 0, \;\; k = 0, 1, \ldots, n-1, \tag{2a}$$

in case of multivalued variables, e.g. $v_r$, they read

$$\frac{\partial^k v_{rn}}{\partial r^k} = 0, \quad n > 0, \;\; k = 0, 1, \ldots, n-2, n. \tag{2b}$$

The cases $n < 0$ follow from the complex conjugate relation with the positive harmonics. The case $n = 0$ gives $v_{z0} = f_{z0}(r^2)$ and $v_{r0} \sim r f_{r0}(r^2)$.

Conditions (2) are a consequence of assuming that the solution is infinitely differentiable and that the singular axis is a regular point of the Cartesian system of coordinates [7]. When all these conditions are not properly included, the regularity of the solution is not guaranteed. The problem is commonly overcome in analytical approaches by simply neglecting the solution that are divergent at the axis; in a numerical solution small errors excite the unphysical terms that are divergent and eventually invalidate the calculation. However, all constraints (2) cannot be imposed when solving the equations (1) that require only the evaluation of the first and second order derivatives.

To overcome this difficulty, we define scaled variables that automatically behave correctly as $r \to 0$ and implicitly satisfy the conditions (2), as follows. The scaled vector function $\mathbf{g} = \{g_z, g_r, g_\theta\}$ is introduced, whose harmonics are related to those of the velocity field by (the time dependence is omitted for brevity)

$$v_{kn}(z, r) = g_{kn}(z, r) r^{|n|-1} \quad n \neq 0, \tag{3a}$$

where the subscript $k$ means $\{z, r, \theta\}$, and $n$ is the harmonic. The satisfaction of (2) then follows from the conditions at $r = 0$:

$$g_{zn} = 0, \quad \frac{\partial g_{rn}}{\partial r} = \frac{\partial g_{\theta n}}{\partial r} = 0 \quad n \neq 0, \tag{3b}$$

conditions (3b) give at the leading order $g_{zn} \sim ar$, $g_{rn} \sim b + cr^2$, and $g_{\theta n} \sim \mathrm{i}b + dr^2$, where $a$, $b$, $c$, and $d$ are complex functions of $z$. It must be noticed that the coefficients of the radial and azimuthal components are related in order to automatically satisfy the incompressibility at the axis. The present scaling is equivalent to that proposed in [7] for the single-valued function $v_z$, $v_{zn} = f_n(r^2)r^{|n|}$, when $g_{zn} \sim r$. Following the same line, a pseudo-potential $Q$ is introduced

$$\phi_n(z, r) = Q_n(z, r)r^{|n|} \quad n \neq 0, \tag{4a}$$

with the condition

$$\frac{\partial Q_n}{\partial r} = 0 \quad \text{at } r = 0. \tag{4b}$$

A scaled-vorticity vector $\mathbf{q}$ is also used

$$\omega_{kn}(z, r) = q_{kn}(z, r)r^{|n|-2} \quad n \neq 0, \tag{5a}$$

with pole conditions which automatically derive from those of the $\mathbf{g}$ field:

$$q_{kn} = 0 \quad \text{at } r = 0. \tag{5b}$$

The variable $\mathbf{q}$ can also be defined using the same scaling of the field (3a), varying consequently the conditions at $r = 0$. For the zeroth mode, the formulation in term of primitive variable is maintained.

The Navier–Stokes equation (1a) can be rewritten in terms of scaled variables as

$$\begin{aligned}
&\frac{\partial g_{zn}}{\partial t} + NL_{zn} = -\frac{\partial (rQ_n)}{\partial z} + \frac{1}{Re}\left(\frac{1}{r}\frac{\partial q_{\theta n}}{\partial r} + (n-1)\frac{q_{\theta n}}{r^2} - \frac{\mathrm{i}nq_{rn}}{r^2}\right),\\
&\frac{\partial g_{rn}}{\partial t} + NL_{rn} = -\frac{\partial (rQ_n)}{\partial r} - (n-1)Q_n + \frac{1}{Re}\left(\frac{\mathrm{i}nq_{zn}}{r^2} - \frac{1}{r}\frac{\partial q_{\theta n}}{\partial z}\right),\\
&\frac{\partial g_{\theta n}}{\partial t} + NL_{\theta n} = -\mathrm{i}nQ_n + \frac{1}{Re}\left(\frac{1}{r}\frac{\partial q_{rn}}{\partial z} - (n-2)\frac{q_{zn}}{r^2} - \frac{1}{r}\frac{\partial q_{zn}}{\partial r}\right),
\end{aligned} \tag{6}$$

where the $NL_{rn}$ term is

$$NL_{rn} = \frac{1}{r^2}\sum_{\substack{m,j \\ m+j=n}} (g_{zn}q_{\theta j} - q_{zn}g_{\theta j})r^{|m|-m}r^{|j|-j}, \tag{7}$$

and analogous expressions hold for the other components. In (6), a formal gradient operator for the $Q$ field is introduced; an analogous divergence operator can be defined for $\mathbf{g}$ to impose the incompressibility (1b)

$$(\nabla \cdot \mathbf{g})_n = \frac{1}{r}\left(\frac{\partial (rg_{rn})}{\partial r} + \frac{\partial (rg_{zn})}{\partial z} + \mathrm{i}ng_{\theta n} + (n-1)g_{rn}\right) = 0. \tag{8}$$

The set of equations (6)–(8) in terms of scaled variables, with boundary conditions (3b), (4b) and (5b) at $r = 0$, is equivalent to equations (1) with the high order boundary conditions (2).

## 3. Numerical method

The mathematical formulation reported in Section 2 has been numerically implemented. In the meridian plane, the flow equations are discretised on a face centred staggered grid with standard second order finite-differences. The time advancement is performed with a fractional step method following the methodology described in Verzicco and Orlandi [4], which computes the intermediate non-soleinodal field using the current irrotational contribution. The intermediate field $\hat{\mathbf{g}}$ is obtained using a low-storage third-order Runge–Kutta scheme [17]. Once the intermediate field $\hat{\mathbf{g}}$ is known, the mass conservation law is enforced solving a Poisson-type equation for the corrections $\mathscr{F}_n$ of the pseudo-potential harmonics $Q_n$. In term of the discrete divergence and gradient operators, $\mathscr{D}$ and $\mathscr{G}$ respectively, we have:

$$\mathscr{D}\hat{\mathbf{g}}_n = \mathscr{D}\mathscr{G}(\mathscr{F}_n(t+\Delta t)),$$

$$g_{kn}(t+\Delta t) = \hat{g}_{kn}(t) - \mathscr{G}_k(\mathscr{F}_n(t+\Delta t)),$$

$$Q_n(t+\Delta t) = Q_n(t) + \mathscr{F}_n(t+\Delta t) + O(\Delta t/Re),$$

the subscripts $n$ and $k$ have the same meaning of those in equation (3a). It must be noticed that the evolving equation (6) requires the evaluation of the scaled vorticity field $\mathbf{q}$; therefore, the discrete curl operator $\mathscr{C}$, which is applied to $\mathbf{g}$ and gives the $\mathbf{q}$ field, is defined congruently to the discrete gradient operator $\mathscr{G}$ in order to satisfy the differential identity $\mathscr{C}(\mathscr{G}h)$, where $h$ is an arbitrary scalar field. The placement of the variables within the computational cell is reported in Fig. 1.

The non-linear term (7) is evaluated with a direct convolution in the Fourier space or, alternatively, in the physical domain using a zero-padding technique [18], giving indistinguishable results; the method is selected to optimise the speed depending on the number of harmonics which are effectively solved. As an example, if the computational cells in the meridian plane are $[N_z \times N_r] = [160 \times 128]$, and the solved harmonics are $N_\theta = 8$, the direct convolution in the Fourier space requires a CPU time typically equal to 0.08 s, while evaluating the non-linear term in the physical space a CPU time of 0.15 s is needed. The FFT and IFFT routines are internal functions of the MatLab® package, whose language have been used to write the numerical code. Tests of the performances have been made on a PC with a 3.5 GHz processor and having 2 Gbs of RAM.

The boundary-conditions, that depend on the problem under consideration and that will be specified in Section 4, are enforced during the time advancement of the governing equations (6); the component of the $\mathbf{g}$ field normal to the boundaries is explicitly assigned on the computational points, while the condition on the tangential ones, typically a zero normal derivative, are used to evolve the equations at the inner grid points

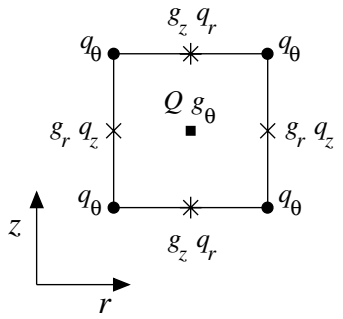


Fig. 1. Sketch of the computational cell.

with the standard methods used for staggered grid [17]. Neumann-type conditions imposed to solve the Poisson problem for $\phi_n$ are rewritten in terms of the pseudopotential $Q_n$.

The time step $\Delta t$ is selected to satisfy the convective and diffusive stability criteria, resulting the latter the more restrictive. The results presented in Section 4 to validate the numerical algorithm have been obtained varying $\Delta t$ between the values $2^{-9}$ and $2^{-10}$. In the case of the pulse entry jet in a cylindrical duct, depending on the different scaling employed, the time step has been varied between $2^{-11}$ and $2^{-12}$.

## 4. Validation of the numerical algorithm

Preliminary tests have been performed to ensure that the normalising procedure does not alter the accuracy of the numerical technique of solution used. To this aim, this approach is applied to a Poisson-type problem on the unitary disk [15], that for the $n$th harmonic $u_n(r)$ reads:

$$r^2 \frac{\mathrm{d}^2 u_n}{\mathrm{d}r^2} + r \frac{\mathrm{d}u_n}{\mathrm{d}r} - n^2 u_n = r^2 f_n(r).$$

This equation has been solved in terms of the normalised variable $g_n$ using the second order scheme employed in the three-dimensional code. Results show that the numerical solution has the same accuracy thorough the domain and, as expected, it is not affected by the normalisation. In Fig. 2 we report the relative error $e_{rel}(N_r)$ in a typical case: $n = 8$, analytical solution $u_n = 2r^8 + r^6 \cos(3\pi r)$, $u_n(1) = 1$; in this case $u_n = g_n r^6$, and $\mathrm{d}g_n/\mathrm{d}r = 0$ at $r = 0$. The error, defined as the mean on the specified domain of the absolute differences between numerical and analytical solutions normalised with the mean of the analytical one, has been computed on the entire domain $0 < r \leqslant 1$ and on its lower and upper halves, varying the number of points $N_r$; the graphs show that the accuracy is second order.

The development of the mathematical formulation and of the numerical method has been stimulated by the interest in several fluid problem of biological interest; typically, these are pulsatile flows in ducts and

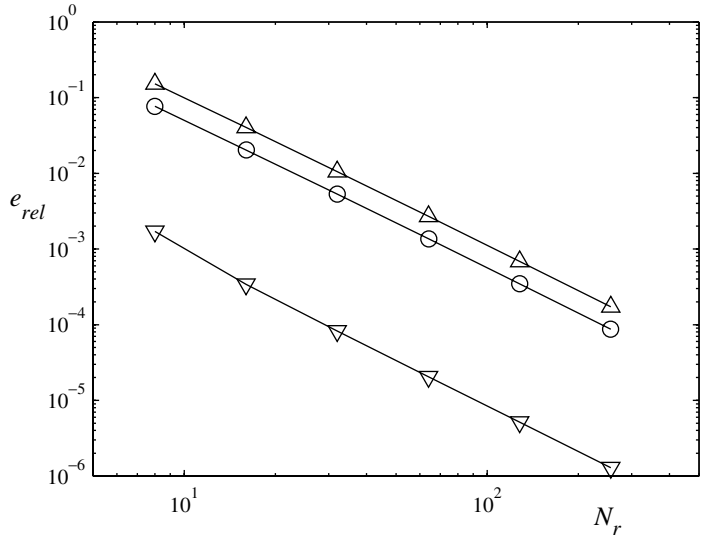


Fig. 2. Relative error between numerical and analytical solution of the Poisson equation on the unitary disk as a function of the number of computational points $N_r$. Average error computed on the domains: (○) $0 < r < 1$, (▽) $0 < r < 0.5$, (△) $0.5 < r < 1$.

chambers, such as the blood flow in the main vessels and in the heart cavity, with low/moderate values of an opportunely defined Reynolds number (details about the physics can be found in Pedrizzetti [19], Baccani et al. [20], Bolzon et al. [21]).

In what follows, we present some tests of validation of the proposed method, where flows in a cylindrical duct with circular cross-section are studied; therefore, the Reynolds number in (1) is $Re = 2UR/\nu$, being $R$ the radius of the tube, and $U$ the axial velocity averaged over a cross-section. Following this scaling, the dimensionless discharge is $\mathcal{Q} = \pi$; in case of a time dependent forcing, such a value is referred to the peak value. The system is forced by imposing an inlet profile to the axial velocity at a given section, say $z = 0$; at the same section, zero normal derivative is imposed to the radial and azimuthal components of the velocity, that is $\partial v_r/\partial z = \partial v_\theta/\partial z$ at $z = 0$. At the wall, $r = 1$, the no-slip condition is imposed. At the outlet section, $z = H$, the axial derivative of the flow variables is set equal to zero, that is a uniform flow is assumed. All these conditions are rewritten in terms of the scaled variables $\mathbf{g}$ and $\mathbf{q}$. Different boundary-conditions can be considered to simulate different physical problem, and/or to improve efficiency of the specific numerical resolution.

From a numerical point of view, a typical length of the computational domain in the $z$-direction is 10, this value has been found to be sufficient not to influence the flow dynamics at $z < 4$; such a length can probably be reduced by the use of more specific boundary-conditions at the outlet section, e.g. a radiative one, to improve computational efficiency. A logarithmic stretching was used in the axial direction to ensure a better resolution close to the inlet section. Also the grid in the $z$-direction has been stretched to capture the boundary-layer growth and its interaction with the inner vorticity dynamics. Several tests have been performed to define the grid resolution in the meridian plane, the results presented in what follows are obtained with $N_r = 128$ and $N_z = 160$; the number of harmonics is $N_\theta = 8$–12.

### 4.1 Test #1

A constant discharge $\mathcal{Q} = \pi$ is assumed; the inlet velocity profile is given by a Poiseuille-type component plus a contribution at the azimuthal wavenumber $n = 1$

$$v_z(0, r, \theta) = 2(1 - r^2) + A(r - r^3)\cos\theta, \tag{9}$$

a value $A = 2$ has been used, so that the first derivative of the profile in the radial direction is equal to zero at $r = 1$ and $\theta = \pi$. The flow is impulsively started from rest, and it is analysed varying the Reynolds number in the range 500–1000. The problem formulation implies the presence of a plane of symmetry; given the profile (9), the symmetry plane passes through $\theta = 0$ and $\theta = \pi$. On this plane, the only non-zero component of the vorticity is $\omega_\theta$, that defines the only non-zero contribution of the three-dimensional vorticity stretching term $\boldsymbol{\omega} \cdot \nabla \mathbf{v}$ when combined with $\partial v_\theta/\partial\theta$. In what follows, the symmetry plane dynamics is presented in terms of $\omega_y$, $y = r\cos\theta$, to simplify the discussion ($\omega_y = \omega_\theta$ at $\theta = 0$, $\omega_y = -\omega_\theta$ at $\theta = \pi$).

The solution at $t = 3$ is reported in Fig. 3, the Reynolds number is $Re = 10^3$ . Far from the inlet, the solution is that of an impulsively started flow in a tube, the flow is irrotational with the exception of the uniform viscous-boundary layer developing at the wall. The $\omega_y$ forced by condition (9) at the inlet enters into the duct for convective effect, giving the defaced field in Fig. 3(a), with the contemporarily development of the other vorticity components. The distribution of the vorticity modulus at $z = 2.35$ is reported in Fig. 3(b). The results do not show any criticality of the flow solution near the axis $r = 0$ that is a regular point in the new formulation.

### 4.2 Test #2

The discharge $\mathcal{Q} = \pi$ is impulsively started at $t = 0$ and then maintained constant until $t = 1$, afterwards the flow is decelerated with an exponential decay, $\mathcal{Q} = \pi\exp(1 - t)$ in order to test the model during flow

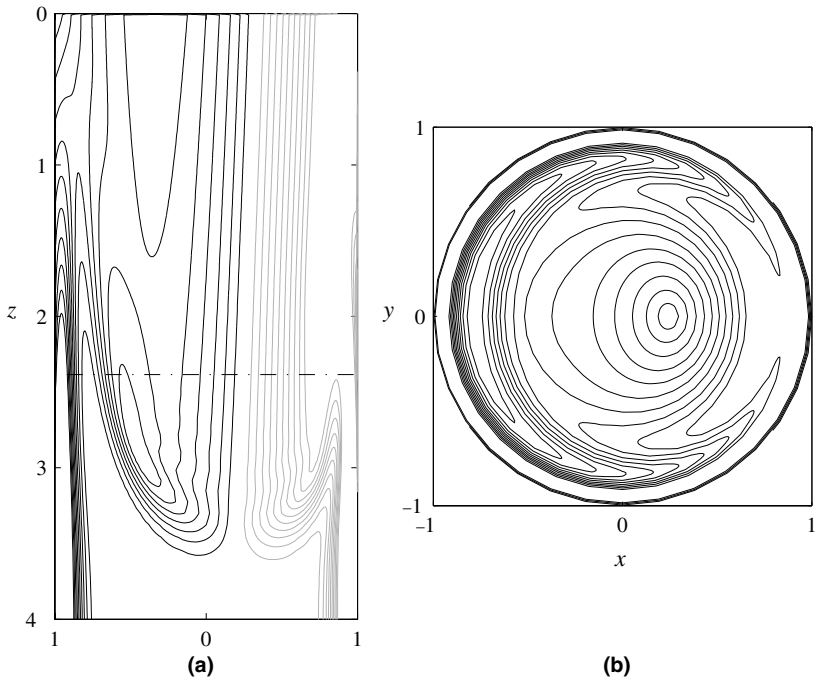


Fig. 3. Impulsively started flow case, $t = 3$, $Re = 10^3$. (a) $\omega_y$ on the symmetry plane, (b) vorticity modulus distribution at $z = 2.35$. Levels from −4 to 4, step 0.4, positive values black, negative values grey.

deceleration, an important issue in physiological flows, and the corresponding accelerated dissipation phenomena. The zeroth mode of the entering velocity $v_{z0}$ is assumed to be a blunt profile, that is constant for $r < r_1 < 1$, and with a parabolic tail to join the no-slip boundary condition at $r = 1$; a contribution like that in (9) is added to the first harmonic. The chosen parameter are $r_1 = 0.4$, $A = 0.5$. The Reynolds number has been varied between 500 and 3000.

At the inlet section, the central region of the duct is characterised by a zero azimuthal vorticity, being the entering $\omega_\theta$ concentrated in a narrow region around $r \simeq 0.5$. The first harmonic is responsible for the eccentricity of the axial velocity profile. As can be observed in Fig. 4(a), $t = 3$ and $Re = 3000$, the solution evolves similarly to the case reported in Fig. 3; the $\omega_y$ distribution on the symmetry plane and the cross-section of the vorticity modulus do not show any presence of the singular axis, giving a smooth solution in the central region of the tube. The axial and radial components of the vorticity, as well as the velocity field, present similar well-behaving distribution at all instants.

Additional tests have been performed. Using the same inlet profile, the flow is forced with turbulent-like velocity distributions. At $t = 0$, the lower harmonics of the **g** field, $n = 0, 1, 2$, are forced with random distributions, with values in the range 0–1; boundary conditions are imposed, and incompressibility is enforced with the same numerical procedure used during all the simulations. In this case $N_\theta = 16$ harmonics are solved. In Fig. 5, we report the $\omega_y$ distributions close to the inlet section. At $t = 0$, the vorticity field shows some signs of symmetry with respect to the central axis, due to the contributions of the forced lower harmonics, Fig. 5(a). During the following evolution, shown in Fig. 5(b)–(d), the trace of such an initial forcing progressively disappears. While the viscous boundary-layer develops at the wall, and the inlet regular vorticity enters the duct, the energy of the forced random field is transferred to the higher harmonics by the non-linear interaction, and it is slowly dissipating. The vorticity field pictures show how this complex evolution progresses without presenting any criticality in the whole domain including across the singular axis.

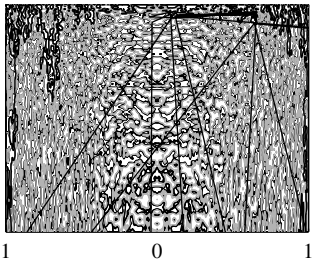
1
0
1

### 4.3 Pulsed entry jet in a cylindrical duct

According to the physical problems which stimulated this study, the described method has been applied to the analysis of a pulsatile jet in a tube, a simplified model for the strongly accelerated flows in the heart chambers and in the main arterial vessels (diastolic phase for the mitral valve, or systolic for the aortic valve, for example, see [19–21] for references). In this context, a different dimensionless formulation is suggested by the physics itself. The natural time scale is the heartbeat period $T$, therefore the pulse jet has a duration approximately equal to half period, and the instant corresponding to the maximum flow rate is fixed here at $t = 0.1$. A velocity scale $U_0$ can be defined as the peak velocity averaged on the inlet cross section. All the variables can be made dimensionless according to these scales, and a Reynolds number is therefore defined as $Re_T = U_0^2 T/\nu$. The dimensionless time profile of $\mathcal{Q}(t)$ is represented by the function

$$\mathcal{Q}(t) = At^2 \exp(-ft), \tag{10}$$

that models the pulsatile flow of typical clinical data; $f = 20$ is the characteristic frequency of the deceleration, and the factor $A = 0.385$ scales the total discharge [20]. The following blunt velocity profile $v_z$ is assigned at the inlet:

$$v_z(0, r, \theta) = C(t)\mathrm{e}^{-\left(\frac{(r\cos\theta-\varepsilon)^2+(r\sin\theta)^2}{\sigma^2}\right)^6}, \tag{11}$$

$\varepsilon$ is the eccentricity of the profile, $\sigma$ controls its steepness, $C$ is the normalisation coefficient to agree with the integral (10).

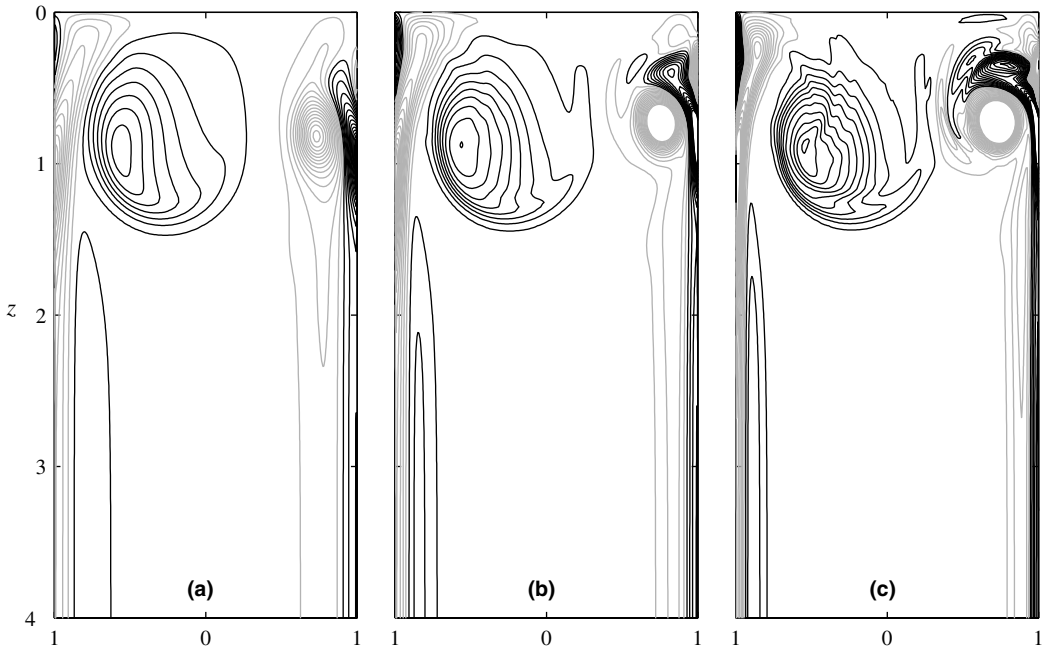


Fig. 6. Pulsatile flow, $t = 0.5$, $\omega_y$ on the symmetry plane. (a) $Re_T = 5 \times 10^3$, (b) $Re_T = 10^4$, (c) $Re_T = 2 \times 10^4$. Levels from −60 to 60, step 4, positive values black, negative values grey.

The Fourier representation of the profile (11) defines the inlet forcing $g_{zn}(0, r, t)$, zero normal derivative is imposed to the radial and azimuthal components of $\mathbf{g}$. As $z \to \infty$, the flow is assumed to be uniform in the $z$-direction. At the duct wall $r = R$, the boundary condition reads $\mathbf{g}(z, R, t) = 0$. At $t = 0$ the flow starts from rest.

The problem has been analysed varying $Re_T$ in the range $[5 \times 10^3$–$2.5 \times 10^4]$, corresponding to a standard Reynolds number $2U_0R^*/\nu \simeq 150$–$750$. The parameter $\sigma$ in Eq. (11) is fixed $\sigma = 2R/3$; the eccentricity has been varied in the range $\varepsilon = [0.05R$–$0.2R]$.

The flow field changes to an increasingly three-dimensional pattern at growing values of eccentricity. For $\varepsilon = 0.05R$ the flow is almost axisymmetric, when eccentricity is increased to $\varepsilon = 0.1R$ and $\varepsilon = 0.2R$ the non-symmetry increases accordingly, without showing the appearance of qualitative differences, in agreement with previous observation under similar conditions [21].

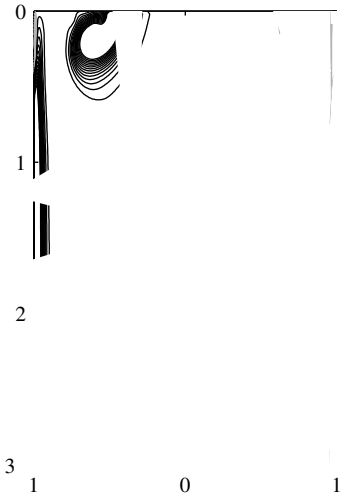

In Fig. 6, the vorticity distributions on the symmetry plane are reported at $t = 0.5$, $\varepsilon = 0.2R$, for the three values of $Re_T = [5, 10, 20] \times 10^3$; the results have been obtained fixing $N_\theta = 8$. At this stage of the evolution, the symmetry plane vorticity shows the complete lack of axial symmetry of the solution. A weak detached vortex can be observed in the left portion of each picture, while a more intense interaction between the entering vorticity and the boundary-layer one appears on the right side. More intense vortex structures are related to the higher value of $Re_T$, Fig. 6(c); in this case small oscillations of the solution are related to the limited azimuthal resolution, being $N_\theta = 8$.

The flow evolution at $Re_T = 20 \times 10^3$, is reported in Fig. 7, as solved with an increased number of harmonics $N_\theta = 12$. During the initial stage of motion, the entry flow develops an eccentric vortex structure, Fig. 7(a) at $t = 0.125$, the remaining part of the flow is irrotational, with the exception of the viscous boundary-layer at the wall. During the following evolution, the vortex structure grows in size and induces an opposite sign vorticity layer at the wall, Fig. 7(b) at $t = 0.25$. Afterwards, the main vorticity structure tends to roll-up; the left portion, $\theta = \pi$, moves toward the centre of the tube, while the right one strongly interacts with the boundary-layer, inducing its separation from the wall surface, and thus forming a three-layer vorticity distribution close to the inlet section, Fig. 7(c) at $t = 0.375$. The final stage of the evolution here reported is characterised by the detachment of the vortex structure; its left part crosses the duct centreline, the right one remains attached to the wall lifting-up the opposite sign vorticity, Fig. 7(d) at $t = 0.5$. The comparison between the cases $N_\theta = 8$ and $N_\theta = 12$ gives about identical solutions up to the final stage where (compare Fig. 6(c) and Fig. 7(d)) some fictitious oscillations found at $N_\theta = 8$, due to the sum-up of energy at the highest modes, are cleared-out in the $N_\theta = 12$ solution although the main features of the flow are unchanged.

A different description of the flow evolution is given in Fig. 8, where the secondary flows at $z \simeq 0.5$ are reported, at the same instants of those of Fig. 7; the computed velocities have been interpolated on a coarse Cartesian grid to better visualise the flow pattern. Until the vortex structure is confined close to the inlet section, the secondary flow is that of a diverging irrotational jet, which tends to occupy the whole cross-section, Fig. 8(a). When the vortex structure develops, it becomes a sort of inclined vortex ring, and its

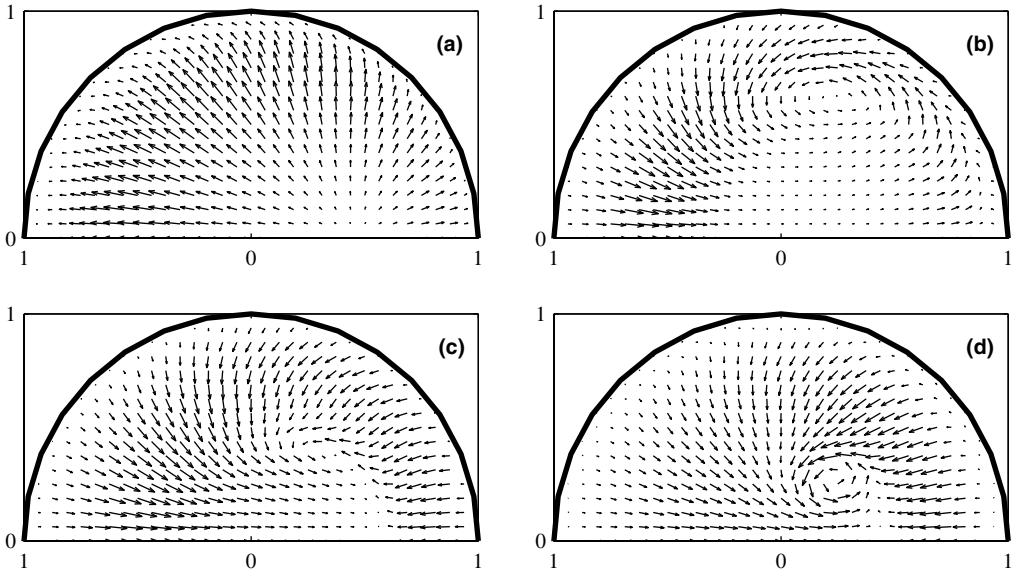


Fig. 8. Pulsatile flow $Re_T = 2 \times 10^4$, secondary flow at $z \simeq 0.5R$. (a) $t = 0.125$, (b) $t = 0.25$, (c) $t = 0.375$, (d) $t = 0.5$.

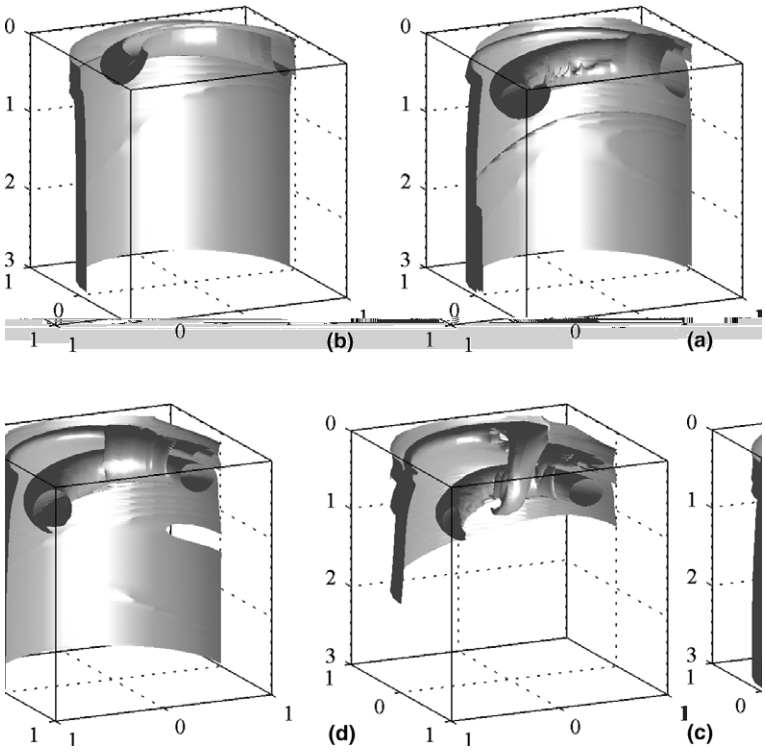


Fig. 9. Pulsatile flow $Re_T = 2 \times 10^4$, isosurfaces of the vorticity modulus. (a) $t = 0.125$, (b) $t = 0.25$, (c) $t = 0.375$, (d) $t = 0.5$. Value: 30.

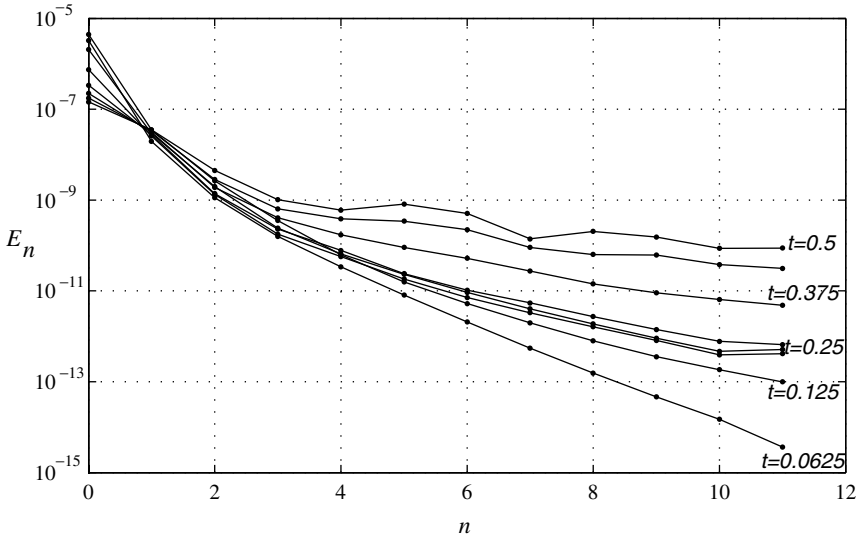


Fig. 10. Pulsatile flow $Re_T = 2 \times 10^4$, $N_\theta = 12$, $E_n(n)$, $t$ from 0.0625 to 0.5, step 0.0625.

geometry induces significant vorticity components along $z$ and $r$ directions [21]. The appearance of $\omega_z$ is represented by the formation of secondary recirculating cells, Fig. 8(b) and (c), whose growth in size and intensity induces an evident transversal flow (from left to right) localised in the vicinity of the symmetry plane, Fig. 8(d). The cross-sectional flow helps in clarifying the transversal motion of the left portion of the vortex structure, described in Fig. 7.

A global view of the wake structure is given in Fig. 9, where the isosurfaces of the vorticity modulus are reported. This description gives a feeling of the three-dimensional evolution of the vorticity field. Initially, the wake is an almost circular vortex ring, dominated by the azimuthal vorticity, Fig. 9(a) at $t = 0.125$. Afterwards, the ring deforms and interacts with the wall boundary-layer (a discussion about the wake-boundary layer reconnection can be found in [21]), Fig. 9(b), $t = 0.25$. In Fig. 9(c) and (d), $t = 0.375$ and $t = 0.5$, a completely three-dimensional vorticity field develops, where the central portion of the flow field becomes dominated by the longitudinal component of the vorticity, $\omega_z$, responsible of the secondary circulation described above.

In order the verify the spectral convergence of the solution, we report in Fig. 10 the kinetic energy associated with each single azimuthal mode $n$, $E_n$, where,

$$E_n = \pi \int_0^H \int_0^R v_n \cdot v_n^* r \, \mathrm{d}z \, \mathrm{d}r, \tag{12}$$

and the asterisk stands for complex conjugate [10]. Such a quantity is computed at eight instants of time, from $t = 0.0625$ to $t = 0.5$, interval $t = 0.0625$. At this highest value of $Re_T$, during the final stage of computation the solution begins to suffer the limitation of the azimuthal resolution, therefore the evolution for $t > 0.5$ is not reported; on the other side, $N_\theta = 12$ appears sufficient to capture the large part of the details of the solution for $t < 0.5$, which has been discussed above.

## 5. Conclusions

The spectral formulation of the Navier–Stokes equations written in the cylindrical system of coordinates requires a number of regularity constraints at the singular axis $r = 0$ that cannot be accounted directly in the solution. The introduction of an appropriate scaling for the harmonics of the primitive variables permits to formulate a mathematical system that is well-posed on the scaled variables and automatically satisfies the regularity conditions at the singular axis. This regularised formulation of the Navier–Stokes equations is of general applicability, however it is particularly useful in the numerical solution of the three-dimensional flow equations in an axisymmetric system of coordinates.

The proposed methodology has been implemented using standard numerical techniques for the spatial and temporal resolution of the equations, in the framework of the spectral/pseudospectral methods. However, the proposed method is independent on its numerical realisation.

Several tests have been performed to prove the ability of the method to solve the flow equations at the singular axis; the system has been typically forced with the lower azimuthal wavenumbers, thus allowing to solve a reduced number of harmonics. Such tests have shown that the solutions behave well close to the singular axis. Afterwards, and as an additional test, the method has been applied to the pulsed entry-jet problem, that is a model for the moderate Reynolds number flows of biological interest, that stimulated the present work. In presence of an eccentric inlet profile, the flow evolution changes from an axisymmetric picture, with a wake vortex sheet possibly detaching to form few vortex rings [19,20], to a fully three-dimensional one.

Results have confirmed the ability of the proposed method to solve the flow about $r = 0$, in fact the singular axis is a regular point in the new formulation. The solution automatically satisfies the regularity conditions at the axis and it is not critical (or it is critical like any boundary) about $r = 0$.

The present method can be easily extended to different systems of coordinates having a polar axis, and the same approach can also be applied to solve different mathematical problems. In such a perspective, it is currently being applied to analyse the three-dimensional flow in a prolate-spheroidal moving cavity, a model for the left ventricular chamber (see [21] and references therein for details).

## Acknowledgements

The work has been partially supported by MIUR (Ministero dell'Istruzione, dell'Università e della Ricerca – Italian Ministry of Education, University, and Research) under the grant FIRB 2001 "Biomedical Fluid Mechanics: diastolic inflow in the left ventricle of the heart and technical synergy for analysis of the vitreous body within the eyeball".

## References

[1] J.C.M. Eggels, F. Unger, M.H. Weiss, J. Westerweel, R.J. Adrian, R. Friedrich, F.T.M. Nieuwstadt, Fully developed turbulent pipe flow: a comparison between direct numerical simulation and experiment, J. Fluid Mech. 268 (1994) 175.
[2] K. Akselvoll, P. Moin, An efficient method for temporal integration of the Navier–Stokes equations in confined axisymmetric geometries, J. Comput. Phys. 125 (1996) 454–463.
[3] B.J. Boersma, G. Brethouwer, F.T.M. Nieuwstadt, A numerical investigation on the effect of the flow conditions on the self-similar region of a round jet, Phys. Fluids 10 (4) (1998) 899.
[4] R. Verzicco, P. Orlandi, A finite-difference scheme for three-dimensional incompressible flows in cylindrical coordinates, J. Comput. Phys. 123 (1996) 402–414.
[5] K. Mohseni, T. Colonius, Numerical treatment of polar coordinate singularities, J. Comput. Phys. 157 (1999) 787–795.
[6] L.S. Tuckerman, Divergence-free velocity fields in nonperiodic geometries, J. Comput. Phys. 80 (1989) 403.
[7] H.R. Lewis, P.M. Bellan, Physical constraints on the coefficients of Fourier expansions in cylindrical coordinates, J. Math. Phys. 31 (11) (1990) 2592–2596.
[8] V.G. Priymak, T. Miyazaki, Accurate Navier–Stokes investigation of transitional and turbulent flows in a circular pipe, J. Comput. Phys. 142 (1998) 370–411.
[9] G.S. Constantinescu, S.K. Lele, A highly accurate technique for the treatment of flow equations at the polar axis in cylindrical coordinates using series expansions, J. Comput. Phys. 183 (2002) 165–186.
[10] J.M. Lopez, F. Marques, J. Shen, An efficient spectral-projection method for the Navier–Stokes equations in cylindrical geometries, J. Comput. Phys. 176 (2002) 384–401.
[11] S.A. Orszag, A.T. Patera, Secondary instability of wall-bounded shear flows, J. Fluid Mech. 128 (1983) 347.
[12] Y. Zhang, A. Gandgi, A.G. Tomboulides, S.A. Orszag, Simulation of pipe flow, in: Symposium on Application of Direct and Large Eddy Simulation to Transition and Turbulence (AGARD Conf., Crete, Greece, 1994), vol. CP-551, pp. 17.1–17.9.
[13] P. Loulou, Direct Numerical Simulation of Incompressible Flow Using a B-Spline Spectral Method, Ph.D. thesis, Department of Aeronautics and Astronautics, Stanford University, 1996.
[14] P. Loulou, R.D. Moser, N.N. Mansour, B.J. Cantwell, Direct numerical simulation of incompressible pipe flow using a B-Spline Spectral Method, NASA Ames Research Center, Technical Memorandum 1997, 110436.
[15] W. Huang, D.M. Sloan, Pole condition for singular problems: the pseudo spectral approximation, J. Comput. Phys. 107 (1993) 254–261.
[16] G.K. Batchelor, An Introduction To Fluid Dynamics, Cambridge University Press, Cambridge, 1967.
[17] P. Orlandi, Fluid Flow Phenomena, Kluwer Academic Publishers, Dordrecht, 2000.
[18] C. Canuto, M.Y. Hussaini, A. Quarteroni, T. Zang, Spectral Methods In Fluid Dynamics, Springer-Verlag, Berlin/New York, 1988.
[19] G. Pedrizzetti, Unsteady tube flow over an expansion, J. Fluid Mech. 310 (1996) 89.
[20] B. Baccani, F. Domenichini, G. Pedrizzetti, Vortex dynamics in a model left ventricle during filling, Eur. J. Mech. B/Fluids 21 (5) (2002) 527.
[21] G. Bolzon, L. Zovatto, G. Pedrizzetti, Birth of three dimensionality in a pulse jet through a circular orifice, J. Fluid Mech. 493 (2003) 209.